Chinese Chemical Letters 37 (2026) 111918

Contents lists available at ScienceDirect

Chinese Chemical Letters

journal homepage: www.elsevier.com/locate/cclet

Multivariate MOF-derived single-atom catalyst with enhanced site accessibility as a bifunctional electrocatalyst for zinc-air batteries

Guoxin Zhang, Shaoqing Feng, Kairen Cheng, Xingxing Li, Jiangxia Tian, Kai Chen*, Huile Jin*, Shun Wang*

Wenzhou Key Lab of Advanced Energy Storage and Conversion, College of Chemistry and Materials Engineering, Wenzhou University, Wenzhou 325035, China

ARTICLE INFO

Article history:
Received 26 July 2025
Revised 18 September 2025
Accepted 28 September 2025
Available online 29 September 2025

Keywords:
Multivariate MOF
Iron single-atom catalyst
Site accessibility
Bifunctional electrocatalyst
Zinc-air battery

ABSTRACT

High-performance bifunctional oxygen electrocatalysts are urgently required for rechargeable zinc-air batteries (ZABs) due to sluggish kinetics of oxygen reduction/evolution reactions (ORR/OER) at the air cathode. In this study, an iron single-atom catalyst (Fe-SAC, FeTCPP@UiO-66–800) is synthesized by direct pyrolysis of a metalloporphyrin-incorporated multivariate MOF. The spatial separation effect of the framework linkers endows Fe-SAC with hierarchical porosity, improved metal utilization efficiency, and enhanced site accessibility by suppressing the metal agglomeration during pyrolysis. Moreover, the possible formation of di- or tri-atomic iron sites facilitates the OER activity *via* the oxide pathway mechanism (OPM), contributing to the excellent bifunctional ORR/OER performance with a ΔE of 0.59 V. Both liquid and flexible ZAB assembled with FeTCPP@UiO-66–800 demonstrate enhanced activity, long-term durability, and anti-deformation ability (340.5 mW/cm^2 peak power density in liquid device). This study presents a novel strategy for preparing MOF-derived SACs with highly accessible single-atom sites, offering a promising route to high-performance energy conversion devices.

© 2026 Published by Elsevier B.V. on behalf of Chinese Chemical Society and Institute of Materia Medica, Chinese Academy of Medical Sciences.

The global pursuit of carbon neutrality has heightened the demands for advanced energy storage systems, spurring research into clean energy technologies that combine high energy density with cost-effectiveness [1,2]. Zinc-air batteries (ZABs) are promising candidates for renewable energy applications, featuring an exceptional theoretical energy density of 1086 Wh/kg, environmental compatibility, and abundant zinc resources [3,4]. Nevertheless, the practical implementation of ZABs is hindered by kinetic limitations in the oxygen reduction reaction (ORR) and oxygen evolution reaction (OER) at the air cathode during discharge/charge cycles [5,6]. Moreover, the current benchmark electrocatalysts for ORR and OER, including Pt and IrO_2/RuO_2, still suffer from their scarcity, high cost, and unsatisfactory catalytic bifunctionality, which impede the practical application of noble-metal electrocatalysts in ZABs. These bottlenecks constrain energy conversion and operational durability, creating urgent demands for noble-metal-free bifunctional electrocatalysts with excellent catalytic activity and long-term durability.

Recent breakthroughs in catalyst engineering have elevated single-atom catalysts (SACs) to a pivotal role in electrocatalysts, leveraging their maximal atomic efficiency and unique coordination environments [7,8]. Metal-nitrogen-carbon (M-N-C) SACs have garnered particular attention as promising alternatives to noble-metal electrocatalysts due to their superior performance in oxygen redox chemistry, resulting from optimized d-orbital electronic configurations [9,10]. Typically, M-N-C synthesis involves high-temperature pyrolysis of metal-, carbon-, and nitrogen-containing mixtures, which often leads to poor metal dispersion owing to the strong tendency of metal atoms to aggregate into nanoparticles without sufficient spatial confinement [11]. Kucernak *et al.* found that the overall utilization of Fe-N_x sites in an Fe-N-C SAC was 4.5 % for ORR [12]. Gifted by periodic arrangement of organic linkers and metal ions and highly porous skeletons, metal-organic frameworks (MOFs) have emerged as feasible self-sacrificing precursors for the synthesis of M-N-C SACs with improved metal dispersion efficiency [13,14]. In particular, zeolite-imidazole framework-8 (ZIF-8) has been excessively investigated as an ideal precursor, where the abundant nitrogen atoms and low-boiling temperature Zn atom (907 °C) could sufficiently trap metal atoms to form highly exposed M-N_x sites [15,16]. By treating with NH_4I vapor, the Fe utilization efficiency of an iron-doped ZIF-8-derived Fe-N-C SAC increased from 6.7 % to 10.3 %, corresponding to a high site density of 2.1×10^{19} sites/g [17]. However, the doped metal

* Corresponding authors.
E-mail addresses: kaichen@wzu.edu.cn (K. Chen), huilejin@wzu.edu.cn (H. Jin), shunwang@wzu.edu.cn (S. Wang).

https://doi.org/10.1016/j.cclet.2025.111918
1001-8417/© 2026 Published by Elsevier B.V. on behalf of Chinese Chemical Society and Institute of Materia Medica, Chinese Academy of Medical Sciences.

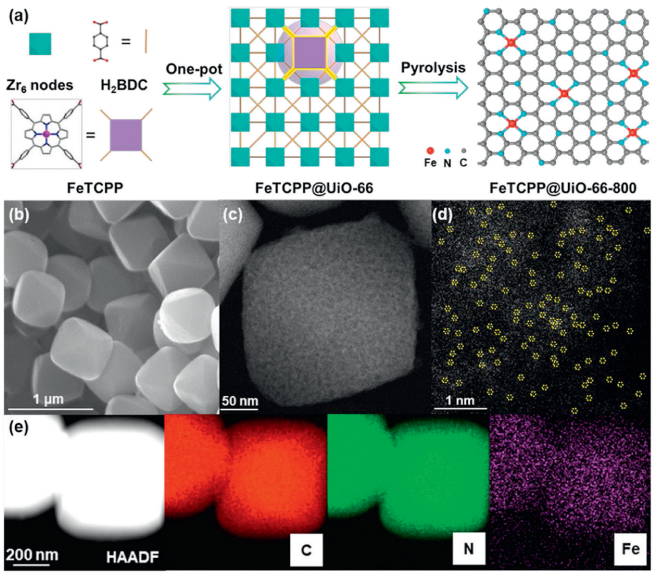


Fig. 1. (a) Schematic presentation for the preparation of FeTCPP@UiO-66–800. (b) SEM, (c) TEM, (d) AC HAADF-STEM images, and (e) corresponding EDS mapping results of FeTCPP@UiO-66–800.

atoms tended to aggregate under the high temperature due to the moderate stability of tetrahedral Fe-N_4 units in ZIF-8 [18]. Recently, innovative strategies employ pre-organized conjugated M-N_4 complexes, such as metallophthalocyanines and metalloporphyrins, as robust molecular templates to promote metal isolation during pyrolysis [19,20]. Significant advances integrate these macrocyclic complexes as rigid linkers in MOF skeletons [21–23]. Jiang's group advanced this approach using a multivariate MOF strategy, achieving a high iron loading of 1.76 wt% in Fe_{SA}-N-C catalysts while preventing iron aggregation by spatial confinement of metal-free porphyrin linkers [24]. This design also established hierarchical porosity with abundant meso–channels, significantly enhancing mass transport and site accessibility, delivering exceptional pH-universal ORR performance. However, fundamental questions persist regarding quantitative metrics to assess metal retention efficiency during pyrolysis and active site accessibility under operational conditions. Moreover, the reliance on excess metal-free porphyrin linkers poses scalability issues due to high costs.

Herein, this study employed a mixed-ligand strategy to synthesize an Fe-N-C SAC by integrating Fe(III) tetra(4-carboxyphenyl)-porphyrin chloride (FeTCPP) into UiO-66, a classic Zr-MOF that was constructed from $[Zr_6O_4(OH)_4]$ nodes and 1,4-benzenedicarbonate (BDC) linkers, where BDC linkers served as spatial partitioners to increase the distance between metalloporphyrins (Fig. 1a). The mixed-ligand architecture enhanced metal dispersion during pyrolysis, suppressing Fe aggregation more effectively than PCN-222(Fe) (built from Zr_6 cluster and FeTCPP linkers) derived Fe-SAC that lacked spatial separation. Textural and kinetic analysis revealed that thermally labile BDC linkers preferentially evacuated after decarboxylation, forming a hierarchically porous carbon matrix with highly accessible Fe-N_4 sites. The optimized catalyst demonstrated exceptional bifunctional performance in ORR/OER, achieving a low potential gap ($\Delta E = 0.59$ V). When implemented as an air cathode catalyst in liquid ZAB, the assembled device delivered a peak power density of 340 mW/cm^2 and sustained for over 700 h at 10 mA/cm^2 with less than 5 % efficiency loss.

The tetracarbonate FeTCPP linker was incorporated into UiO-66 at a FeTCPP/H_2BDC feed ratio of 10 % by direct addition to the precursor solution, followed by hydrothermal synthesis to yield FeTCPP@UiO-66 [25]. The resulting hybrid material exhibited a dark brown color, distinct from the pale white of pristine UiO-66 and the dark black of PCN-222(Fe) (Fig. S1 in Supporting information). Fourier-transform infrared (FT-IR) spectroscopy revealed a characteristic in-plane deformative vibration ($\nu_{Co\text{-}N}$) at 998 cm^{-1} in FeTCPP@UiO-66, confirming successful FeTCPP incorporation (Fig. S2 in Supporting information) [26]. Scanning electron microscopy (SEM) showed that FeTCPP@UiO-66 retained the octahedral morphology of pristine UiO-66, with an average diameter of approximately 800 nm (Fig. S3 in Supporting information). Powder X-ray diffraction (PXRD) analysis demonstrated that FeTCPP@UiO-66 maintained the diffraction patterns of UiO-66, indicating preserved framework periodicity and no phase separation (Fig. S4 in Supporting information). N_2 sorption-desorption isotherms revealed that FeTCPP@UiO-66 exhibited a Brunauer-Emmett-Teller (BET) surface area of 982.0 m^2/g, attributed to sustained adsorption quantity in the micropore regime ($P/P_0 < 0.1$), higher than that of UiO-66 or PCN-222(Fe) (Fig. S6 in Supporting information). The presence of a hysteresis loop confirmed the development of mesopores, suggesting a hierarchical pore structure in FeTCPP@UiO-66. These findings demonstrated the successful incorporation of FeTCPP into UiO-66 without aggregation or disruption of the parent framework.

The hybrid MOF precursor was pyrolyzed at 800 °C under an inert atmosphere and subsequently etched with hydrofluoric acid (HF) solution to remove ZrO_2 and Fe aggregates, yielding Fe-SAC denoted as FeTCPP@UiO-66–800. As shown in Fig. S7 (Supporting information), acid washing completely removed inorganic particles. The diffraction peak at 26.0° was attributed to the (002) lattice plane of graphitized carbon, suggesting that the incorporation of planar metalloporphyrin enhanced carbon matrix graphitization under high temperatures. Raman spectroscopy also confirmed this trend, with FeTCPP@UiO-66–800 exhibiting an I_D/I_G ratio of 0.918, lower than that of UiO-66–800 (0.978) and PCN-222(Fe)-800 (0.924) (Fig. S8 in Supporting information). Additionally, FeTCPP@UiO-66–800 inherited the hierarchical pore structure of the parent MOF, with a BET surface area of 975.4 m^2/g, higher than that of UiO-66–800 (904.4 m^2/g) and PCN-222(Fe)-800 (625.6 m^2/g), facilitating enhanced mass transfer through shorter diffusion pathways and pore-rich architecture (Fig. S9 in Supporting information). The MOF-derived Fe-SACs retained the morphological characteristics of their parent MOFs (Fig. 1b and Fig. S10 in Supporting information). Transmission electron microscope (TEM) images revealed that FeTCPP@UiO-66–800 exhibited a honeycomb-like porous structure, with carbon, nitrogen, and iron elements uniformly distributed across the carbon support (Figs. 1c and e). Aberration-corrected high-angle annular dark-field scanning transmission electron microscopy (AC HAADF-STEM) images confirmed that iron atoms were isolated as single-atom sites without aggregation, as highlighted by yellow circles (Fig. 1d). Inductively coupled plasma optical emission spectroscopy (ICP-OES) analysis showed that the metal loading in PCN-222(Fe)-800 (0.64 wt%) exceeded that of FeTCPP@UiO-66–800 (0.43 wt%), as expected (Table S1 in Supporting information). However, the metal retention percentage for FeTCPP@UiO-66–800, calculated as 9.1 % based on the total iron content in pristine MOFs and corresponding Fe-SACs, was nearly double that of PCN-222(Fe)-800 (4.6 %) (Fig. 2a and Table S1 in Supporting information). Therefore, the spatial separation provided by BDC linkers in FeTCPP@UiO-66 effectively mitigated metal agglomeration during pyrolysis, achieving a higher metal utilization efficiency than PCN-222(Fe).

X-ray photoelectron spectroscopy (XPS) was utilized to characterize the electronic configuration of single-atom iron sites and nitrogen species in Fe-SACs. As depicted in Fig. 2b, the N 1s spectra were deconvoluted into five characteristic peaks: Pyridinic N (398.5 eV), Fe-N_x (399.2 eV), pyrrolic N (400.3 eV), graphitic N (401.2 eV), and oxidized N (402.7 eV) [27]. The presence of Fe-N_x peaks confirmed the inheritance of Fe-N_x sites from Fe-TCPP link-

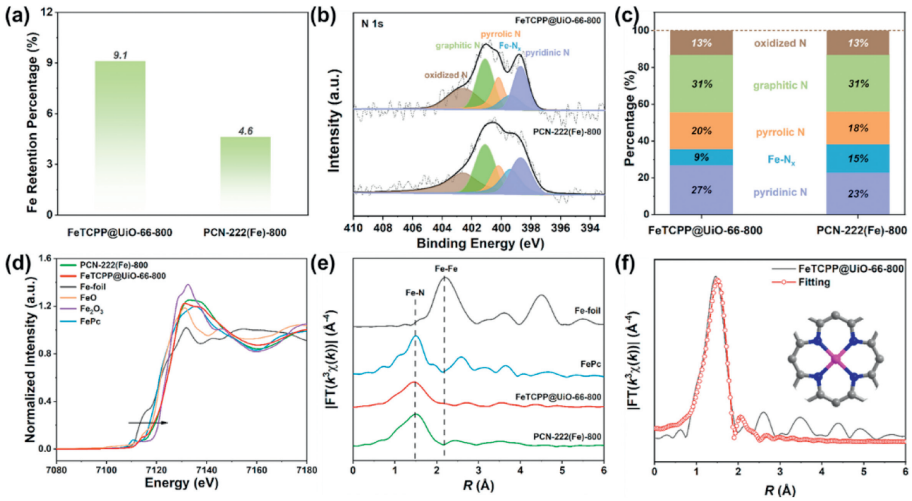


Fig. 2. (a) Fe retention percentage in FeTCPP@UiO-66–800 and PCN-222(Fe)-800 after pyrolysis. (b) High-resolution N 1s XPS spectra and (c) corresponding contents of various nitrogen species. (d) Normalized XANES spectra at Fe K-edge. (e) FT-EXAFS spectra and (f) corresponding fitted curves in *R* space.

ers in both Fe-SACs after pyrolysis. Notably, PCN-222(Fe)-800 exhibited a higher Fe-N_x content (15 %) than FeTCPP@UiO-66–800 (9 %), consistent with the results of ICP-OES (Fig. 2c). X-ray absorption spectroscopy (XAS) at the Fe K-edge further elucidated the electronic configuration of metal sites in Fe-SACs. X-ray absorption near-edge structure (XANES) spectra indicated that the energy absorption thresholds of FeTCPP@UiO-66–800 and PCN-222(Fe)-800 laid between those of FeO and Fe_2O_3, with an average oxidation state of +2.54 and +2.63, respectively (Fig. 2d and Fig. S14 in Supporting information). A pre-edge peak that emerged at 7117 eV, attributed to the 1s to 4pz shake-down transition, confirmed the planar square D_{4h} configuration of Fe-N_x sites in both Fe-SACs [28]. Fourier-transformed k^3-weighted EXAFS (FT-EXAFS) analysis revealed a dominant peak at approximately 1.47 Å for both FeTCPP@UiO-66–800 and PCN-222(Fe)-800, corresponding to the first shell Fe-N scattering path, verifying the successful isolation of iron atoms on the carbon support (Fig. 2e). Moreover, a weak peak at approximately 2.2 Å, assigned to the Fe-Fe scattering path, implying the possible presence of di- or tri-atomic iron sites in FeTCPP@UiO-66–800 [29,30]. Quantitative least-squares EXAFS curve fitting results confirmed that Fe atoms in both FeTCPP@UiO-66–800 and PCN-222(Fe)-800 were both coordinated by four nitrogen atoms (Fe-N_4) with an average bond length of approximately 2.0 Å (Fig. 2f and Fig. S15 in Supporting information). These findings substantiated the presence of identical Fe-N_4 configurations in FeTCPP@UiO-66–800 and PCN-222(Fe)-800, indicating that the mixed-ligand strategy preserved structural symmetry in Fe-N_x sites due to the conjugated system of pre-constructed FeTCPP molecules.

The performance of rechargeable ZABs predominantly depends on the ORR/OER activity of cathode catalysts. The bifunctional oxygen electrocatalytic performance of Fe-SACs was evaluated in an O_2-saturated KOH solution, using commercial Pt/C and RuO_2 as benchmarks. As depicted in Fig. 3a, FeTCPP@UiO-66–800 exhibited a half-wave potential ($E_{1/2}$) of 0.91 V *vs.* RHE, surpassing PCN-222(Fe)-800 (0.87 V) and Pt/C (0.85 V). The fitted Tafel slopes for FeTCPP@UiO-66–800, PCN-222(Fe)-800, and Pt/C were 72.4, 82.1, and 166.5 mV/dec, respectively, demonstrating superior ORR kinetics for FeTCPP@UiO-66–800 (Fig. 3b). Additionally, FeTCPP@UiO-66–800 afforded mass activity of 3480 A/g_{metal} and an apparent turnover frequency (TOF) of 0.50 s^{-1} at 0.9 V *vs.* RHE, outperforming PCN-222(Fe)-800 (670 A/g_{metal} and 0.10 s^{-1}) and Pt/C (14.1 A/g_{metal} and 0.01 s^{-1}) (Fig. 3c). Considering that PCN-222(Fe)-800 possessed similar Fe-N_4 sites and higher metal loading, the origin of enhanced performance for FeTCPP@UiO-66–800 was elucidated by double-layer capacitance (C_{dl}) and electrochemical stripping experiments. The C_{dl} value of FeTCPP@UiO-66–800 was estimated to be 44.2 mF/cm^2, which was higher than that of PCN-222(Fe)-800 (37.7 mF/cm^2) (Fig. S19 in Supporting information). The accessible site density (MSD) of Fe-N_x sites was determined by the electrochemical nitrite adsorption/stripping method in a 0.5 mol/L sodium acetate buffer (pH 5.2), as reported by Kucernak *et al.* [12]. As shown in Fig. S20 (Supporting information), a pronounced reduction peak was observed in the stripping voltammetry plot of FeTCPP@UiO-66–800, compared with PCN-222(Fe)-800. The corresponding accessible MSD value was determined as 2.38 μmol/g for FeTCPP@UiO-66–800, significantly higher than that of PCN-222(Fe)-800 (0.66 μmol/g) (Fig. 3d). The corresponding iron site utilization was calculated to be 3.09 % for FeTCPP@UiO-66–800, demonstrating a nearly six-fold enhancement compared to that of PCN-222(Fe)-800 (0.58 %). Moreover, the intrinsic $TOF_{5.2}$, calculated based on the accessible active sites in the sodium acetate buffer, was determined as 0.25 s^{-1} for FeTCPP@UiO-66–800 and 0.31 s^{-1} for PCN-222(Fe)-800 at 0.9 V *vs.* RHE, respectively. The comparable $TOF_{5.2}$ values verified the identical intrinsic activity of Fe-N_4 sites in two catalysts. To evaluate the performance of non-ferrous sites in ORR, iron-free H_2TCPP@UiO-66–800 and PCN-222(H_2)-800 catalysts were prepared by replacing FeTCPP with H_2TCPP. As shown in Fig. S21 (Supporting information), the H_2TCPP@UiO-66–800 and PCN-222(H_2)-800 afforded a moderate alkaline ORR activity with an $E_{1/2}$ of 0.81 V and 0.72 V (*vs.* RHE), respectively, indicating that the Zr species, along with nitrogen species in the carbon supports, contributed limited activity to the overall ORR activities. Interestingly, the enhanced ORR activity for H_2TCPP@UiO-66–800 compared with PCN-222(H_2)-800 might result from the improved accessibility of active sites. The above results emphasized the efficiency of the multivariate-ligand strategy in enhancing iron site utilization and accessibility within porous carbon, likely due to the larger electrochemical active surface area (ECSA) in FeTCPP@UiO-66–800. Electrochemical impedance spectroscopy (EIS) analysis revealed that FeTCPP@UiO-66–800 displayed a lower charge-transfer resistance (R_{ct} = 25.7 Ω) than PCN-222(Fe)-800 (R_{ct} = 26.9 Ω) in the fitted Nyquist plot, thereby facilitating the charge transfer in the electrocatalytic process (Fig. S22 in Supporting information). Rotating ring-disk electrode (RRDE) measurement confirmed a dominant four-electron ORR pathway for FeTCPP@UiO-66–800, with an electron transfer number (n) of 3.7 in the potential range of 0.3–0.8 V *vs.* RHE (Fig. S24 in Supporting information). Besides,

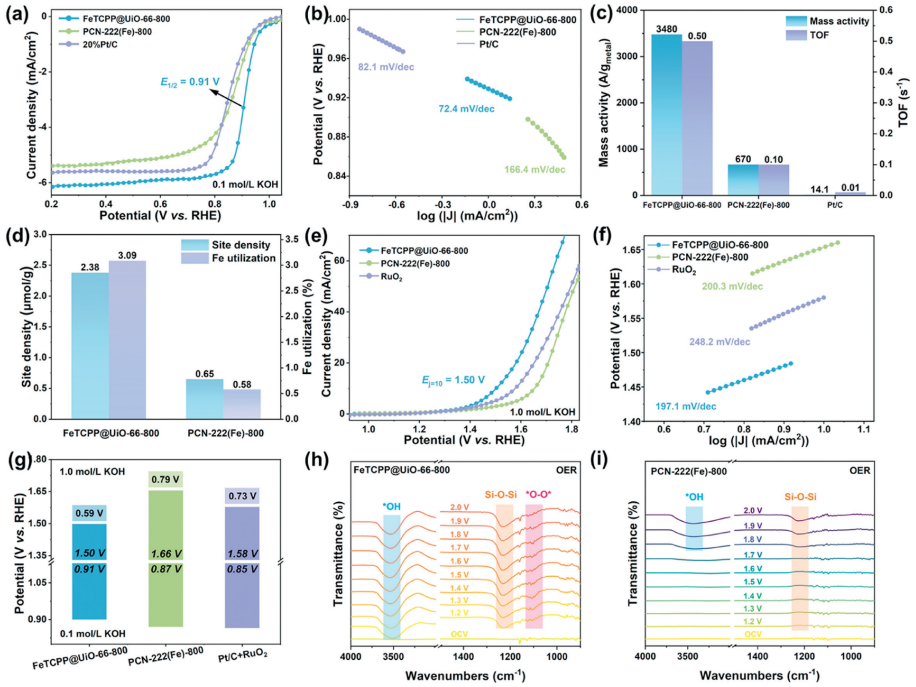


Fig. 3. (a) ORR LSV curves in O_2-saturated 0.1 mol/L KOH solution and (b) corresponding Tafel plots. (c) Mass activity and TOF at 0.9 V *vs.* RHE. (d) Site density and Fe utilization efficiency determined by the nitrite stripping method. (e) OER LSV curves in O_2-saturated 1.0 mol/L KOH solution and (f) corresponding Tafel plots. (g) Comparison of bifunctional ΔE values. *In situ* ATR-IRAS spectra of (h) FeTCPP@UiO-66–800 and (i) PCN-222(Fe)-800 at different potentials in OER.

the long-term stability of FeTCPP@UiO-66–800 was evaluated to provide a useful perspective for practical applications. Only a slight negative shift of 38 mV was observed for FeTCPP@UiO-66–800 after the accelerated degradation test with 6000 cycles (Fig. S25 in Supporting information). The robust stability of FeTCPP@UiO-66–800 could also be validated by an 8.1 % current loss after 10 h of amperometry testing, whereas Pt/C suffered 34.4 % current loss under identical reaction conditions (Fig. S26 in Supporting information). Furthermore, FeTCPP@UiO-66–800 showed excellent methanol tolerance, with no significant performance decay, whereas Pt/C was nearly deactivated upon methanol addition (Fig. S27 in Supporting information). The poisoning effect of SCN^-, evidenced by a 37 mV $E_{1/2}$ decline, confirmed that atomic Fe sites were the primary active centers (Fig. S28 in Supporting information).

For OER performance, FeTCPP@UiO-66–800 achieved a current density of 10 mA/cm^2 at potential ($E_{j=10}$) of 1.50 V *vs.* RHE in 1.0 mol/L KOH, outperforming PCN-222(Fe)-800 (1.66 V) and RuO_2 (1.58 V) (Fig. 3e). According to the data shown in Fig. 3f, the corresponding Tafel slope of FeTCPP@UiO-66–800 was fitted to 197.1 mV/dec, which was comparable to that of PCN-222(Fe)-800 (200.3 mV/dec) but much smaller than RuO_2 (248.2 mV/dec). Moreover, 87.2 % of the initial OER current was retained after 10 h of consistent testing, while a 42.8 % loss of current was observed for RuO_2, implying the excellent practical stability for FeTCPP@UiO-66–800 (Fig. S29 in Supporting information). The iron-free H_2TCPP@UiO-66–800 and PCN-222(H_2)-800 catalysts exhibited similar OER activity with $E_{j=10}$ at approximately 1.6 V (*vs.* RHE), suggesting the predominant role of Fe-N_4 sites in OER (Fig. S30 in Supporting information). The PXRD and XPS analysis revealed that no aggregates were formed after ORR/OER stability tests, suggesting the excellent stability of FeTCPP@UiO-66–800 under practical working conditions (Figs. S31 and S32 in Supporting information). As shown in Fig. 3g, FeTCPP@UiO-66–800 demonstrated exceptional bifunctional ORR/OER activity, as evidenced by a remarkably small potential gap (ΔE) of 0.59 V, which is widely recognized as an essential indicator for bifunctional oxygen electrocatalysts that is defined as the potential gap between $E_{1/2}$ and $E_{j=10}$. This performance surpassed that of PCN-222(Fe)-800 (0.79 V), noble-metal benchmarks (0.73 V), and most reported transition-metal-based SACs (Table S5 in Supporting information), highlighting the advantages of the multivariate MOF strategy.

To gain a deep understanding of the electrocatalytic OER mechanism, *in situ* potential-dependent attenuated total reflection infrared adsorption spectroscopy (ATR-IRAS) was employed to identify the oxygen-containing intermediates at the solid-liquid interface under operating conditions. The predominant broad peak centered at 1240 cm^{-1} was attributed to the Si-O-Si stretching vibration of the ATR crystals (Fig. 3h) [31]. Distinctive vibration frequencies at approximately 1100 cm^{-1} emerged as the applied potential gradually increased from 1.2 V to 1.4 V (*vs.* RHE), which was attributed to the bridging oxygen configuration at the dual active sites [32,33]. The detected key *O–O* intermediate would simultaneously form a characteristic M-*O–O*-M configuration, suggesting that FeTCPP@UiO-66–800 followed an OPM pathway on di- or tri-atomic sites. Moreover, the potential-dependent broad peak at approximately 3500 cm^{-1} that was attributed to another key intermediate of *OH also verified the OPM pathway in OER. For comparison, *in situ* ATR-IRAS measurements were also performed on PCN-222(Fe)-800 (Fig. 3i). However, no apparent peaks regarding the oxygen intermediates were found due to its inferior OER activity. Compared to PCN-222(Fe) with robust skeletons, the parent UiO-66 constructed by light BDC linkers tended to shrink under high temperature to shorten the distance between iron sites, thereby improving the OER activity *via* the OPM pathway.

The enhanced accessibility of Fe-N_4 sites and excellent bifunctional ORR/OER activity highlighted FeTCPP@UiO-66–800 as a promising air cathode catalyst in rechargeable ZABs. The practical application was assessed in a self-assembled liquid ZAB using FeTCPP@UiO-66–800 as the air cathode, zinc foil as the anode, and a mixed solution containing 6 mol/L KOH and 0.2 mol/L $Zn(OAc)_2$ as electrolyte. The liquid ZAB device with FeTCPP@UiO-66–800 exhibited a stable open-circuit voltage (OCV) of 1.42 V

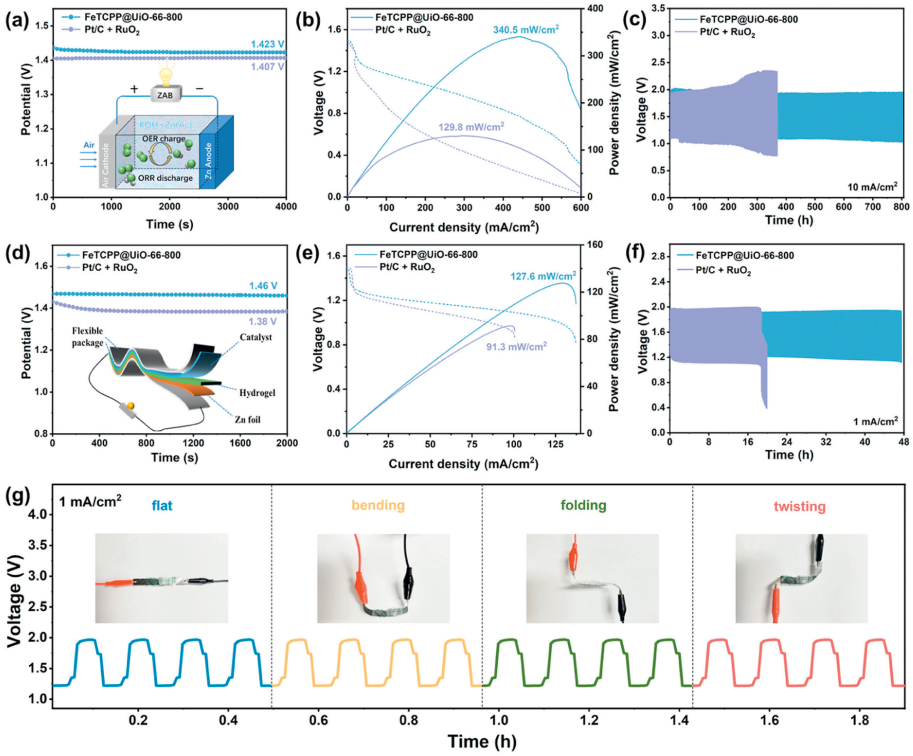


Fig. 4. Graphical illustration of (a) liquid and (d) flexible ZAB and corresponding OCV plots. (b, e) Polarization and power density diagrams, and (c, f) galvanostatic charge-discharge cycle curves in liquid and flexible ZABs, respectively. (g) Cycling stability of FeTCPP@UiO-66–800-assembled flexible ZAB under different deformations.

and superior discharge performance, achieving a peak power density of 340.5 mW/cm^2, surpassing noble-metal benchmarks (1.40 V and 129.8 mW/cm^2) (Figs. 4a and b). Furthermore, the Fe-SAC-loaded ZAB demonstrated a specific capacity of 702.9 mAh/g_{Zn} at 10 mA/cm^2, exceeding that of Pt/C + RuO_2 (626.2 mAh/g_{Zn}) (Fig. S33a in Supporting information). Galvanostatic discharge tests at various current densities showed that FeTCPP@UiO-66–800 exhibited higher discharge voltages than the Pt/C + RuO_2 catalyst, indicating its superior rate performance (Fig. S33b in Supporting information). Long-term durability tests, conducted *via* galvanostatic cycling at 10 mA/cm^2 with each cycle lasting for 10 min, suggested that the FeTCPP@UiO-66–800-based ZAB sustained exceptional stability over 700 h, maintaining a constant voltage gap of 0.87 V (Fig. 4c). Furthermore, a lifespan of more than 144 h was achieved for FeTCPP@UiO-66–800 even under a higher current density of 25 mA/cm^2 (Fig. S34 in Supporting information). In contrast, the noble metal catalyst, despite an initial voltage gap of 0.85 V, degraded rapidly and failed after 200 h at 10 mA/cm^2. The above results established FeTCPP@UiO-66–800 as a highly competitive alternative to noble-metal benchmarks in liquid ZABs, outperforming most of the reported transition-metal SACs (Table S7 in Supporting information).

Encouraged by the development of flexible energy storage devices, a flexible ZAB was fabricated using FeTCPP@UiO-66–800-deposited carbon cloth as the air cathode, alkaline gel of polyacrylic acid (PAA/KOH) as the *quasi*-solid-state electrolyte, and zinc foil as the anode, achieving an OCV of 1.46 V, higher than that of Pt/C + RuO_2 (1.38 V) (Fig. 4d) [34]. The flexible ZAB also exhibited higher peak power density (127.6 mW/cm^2), specific capacity (761.1 mAh/g_{Zn} at 1 mA/cm^2), rate performance, and galvanostatic charging-discharging durability compared to noble-metal counterparts (Figs. 4e and f, Fig. S35 in Supporting information). Mechanical flexibility was evaluated under bending, folding, and twisting, with negligible changes in the charging (1.96 V) and discharging (1.22 V) plateaus at 1 mA/cm^2, underscoring the excellent anti-deformation performance and practical viability for FeTCPP@UiO-66–800 (Fig. 4g). After folding and unfolding for 500 times, a slightly reduced charge voltage was observed for flexible ZAB, demonstrating its moderate deformation stability (Fig. S36 in Supporting information). To evaluate the temperature tolerance, we measured the performance of FeTCPP@UiO-66–800-assembled flexible ZAB in a wide temperature range of −20∼60 °C (Fig. S37 in Supporting information) [35,36]. When the operating temperature dropped to −20 °C, the flexible ZAB delivered a prolonged lifespan of more than 160 h at a current density of 1.0 mA/cm^2, while the discharge voltage and power density dramatically deteriorated under low temperature due to the slow ion migration in the *quasi*-solid-state electrolyte. However, the flexible ZAB failed the discharge/charge cycling tests in a few hours at 60 °C, which possibly resulted from the detached solid-solid interface between electrolyte and cathode. Future work will focus on employing hydrogels with enhanced conductivity and stability under wide operating temperatures to improve the potential application of flexible ZAB outdoors.

Therefore, the well-designed spatial separation strategy endowed the derived Fe-SAC with desired hierarchical porosity and highly exposed Fe-N_4 sites, resulting in the remarkable bifunctional electrocatalytic activity and device performance. However, the limited metal loadings and unsatisfactory stability remained as critical challenges in advancing electrocatalytic performance. We failed to increase the metal loading by magnifying the dosage of FeTCPP in the UiO-66. The FeTCPP linkers tended to form PCN-222(Fe) when the FeTCPP/H_2BDC feed ratio increased to 20 %, as needle-like rods were detected in SEM images with UiO-66 decorated on the external surface (Fig. S38 in Supporting information). On the other hand, the highly exposed single-atom iron sites were also expected to be attacked by oxidative radicals, leading to inevitable iron dissolution. Rational design of single-atom sites with robust binding

interactions between metal atoms and carbon support is urgently needed.

In summary, an iron single-atom catalyst with highly accessible Fe-N_x sites was synthesized by direct pyrolysis of a metalloporphyrin-incorporated MOF precursor. The spatial separation effect of the framework linkers effectively suppressed metal aggregation during pyrolysis, resulting in enhanced accessible site density and metal utilization efficiency. Benefited from the hierarchical porous structures, the close interaction between single-atom Fe-N_4 sites in FeTCPP@UiO-66–800 promoted the OER process *via* an OPM pathway, demonstrating exceptional bifunctional ORR/OER activity with a small ΔE of 0.59 V and outstanding practical performance in both liquid and *quasi*-solid-state flexible ZABs. This work provided valuable insights for the preparation of MOF-derived SACs with superior catalytic performance through tailored structure design.

Declaration of competing interest

The authors declare that they have no known competing financial interests or personal relationships that could have appeared to influence the work reported in this paper.

CRediT authorship contribution statement

Guoxin Zhang: Writing – original draft, Visualization, Methodology, Investigation, Data curation. **Shaoqing Feng:** Validation, Investigation, Data curation. **Kairen Cheng:** Investigation, Data curation. **Xingxing Li:** Investigation, Data curation. **Jiangxia Tian:** Investigation, Formal analysis. **Kai Chen:** Writing – review & editing, Supervision, Project administration, Funding acquisition, Conceptualization. **Huile Jin:** Writing – review & editing, Funding acquisition. **Shun Wang:** Writing – review & editing, Funding acquisition.

Acknowledgment

The authors acknowledged the financial support provided by the National Natural Science Foundation of China (Nos. 52102294, 52331009, 52272088).

Supplementary materials

Supplementary material associated with this article can be found, in the online version, at doi:10.1016/j.cclet.2025.111918.

References

[1] J. Suntivich, H.A. Gasteiger, N. Yabuuchi, et al., Nat. Chem. 3 (2011) 546–550.
[2] Y.Y. Dai, C.M. Xu, X.H. Liu, et al., Carbon Energy 3 (2021) 253–270.
[3] J.N. Liu, C.X. Zhao, J. Wang, et al., Energy Environ. Sci. 15 (2022) 4542–4553.
[4] D. Yang, D. Chen, Y. Jiang, et al., Carbon Energy 3 (2021) 50–65.
[5] P. Chen, T. Zhou, L. Xing, et al., Angew. Chem. Int. Ed. 56 (2017) 610–614.
[6] S. Qu, J. Liu, X. Han, et al., Carbon Energy 4 (2022) 867–877.
[7] J. Yang, W. Li, D. Wang, et al., Adv. Mater. 32 (2020) 2003300.
[8] K. Liu, J. Fu, Y. Lin, et al., Nat. Commun. 13 (2022) 2075.
[9] B. Singh, M.B. Gawande, A.D. Kute, et al., Chem. Rev. 121 (2021) 13620–13697.
[10] Y. Shang, X. Xu, B. Gao, et al., Chem. Soc. Rev. 50 (2021) 5281–5322.
[11] J. Fang, Q. Chen, Z. Li, et al., Chem. Commun. 59 (2023) 2854–2868.
[12] D. Malko, A. Kucernak, T. Lopes, Nat. Commun. 7 (2016) 13285.
[13] Z. Song, L. Zhang, K. Doyle-Davis, et al., Adv. Energy Mater. 10 (2020) 2001561.
[14] L. Hu, C. Dai, L. Chen, et al., Angew. Chem. Int. Ed. 60 (2021) 27324–27329.
[15] X. Li, A.E. Surkus, J. Rabeah, et al., Angew. Chem. Int. Ed. 59 (2020) 15849–15854.
[16] Z. Li, Y. Chen, S. Ji, et al., Nat. Chem. 12 (2020) 764–772.
[17] J. Liu, Y. Liu, B. Nan, et al., Angew. Chem. Int. Ed. 64 (2025) e202425196.
[18] Q. Wang, T. Ina, W.T. Chen, et al., Sci. Bull. 65 (2020) 1743–1751.
[19] Y. Liu, H. Zhou, C. Jin, et al., Appl. Catal. B: Environ. 338 (2023) 123061.
[20] B. Bayarkhuu, H. Cho, G. Cho, et al., Adv. Funct. Mater. 35 (2025) 2411661.
[21] L. Jiao, R. Zhang, G. Wan, et al., Nat. Commun. 11 (2020) 2831.
[22] L. Jiao, W. Yang, G. Wan, et al., Angew. Chem. Int. Ed. 59 (2020) 20589–20595.
[23] Y. Zhang, H. Han, J. Qin, et al., J. Porphyr. Phthalocyan. 25 (2021) 878–884.
[24] L. Jiao, G. Wan, R. Zhang, et al., Angew. Chem. Int. Ed. 57 (2018) 8525–8529.
[25] M. Ni, M. Gong, X. Li, et al., Appl. Mater. Today 23 (2021) 100982.
[26] Y.H. Zhang, W. Zhao, J. Wang, et al., Spectrochim. Acta A 75 (2010) 499–506.
[27] M. Xie, J. Wang, X.L. Du, et al., RSC Adv. 12 (2022) 32518–32525.
[28] M. Liu, Y. Liu, X. Zhang, et al., Angew. Chem. Int. Ed. 64 (2025) e202504923.
[29] Y.X. Zhang, S. Zhang, H. Huang, et al., J. Am. Chem. Soc. 145 (2023) 4819–4827.
[30] X. Wang, L. Xu, C. Li, et al., Nat. Commun. 14 (2023) 7210.
[31] Y. Xue, J. Zhao, L. Huang, et al., Nat. Commun. 14 (2023) 8093.
[32] Q. Ji, B. Tang, X. Zhang, et al., Nat. Commun. 15 (2024) 8089.
[33] C. Lin, J.L. Li, X. Li, et al., Nat. Catal. 4 (2021) 1012–1023.
[34] F. Gu, W. Guo, Y. Yuan, et al., Adv. Mater. 36 (2024) 2313096.
[35] J. Wang, Z. Wang, Y. Chen, et al., J. Energy. Chem. 106 (2025) 823–831.
[36] S. He, S. Gao, S. Hu, Energy Stor. Mater. 77 (2025) 104194.